Tropical Cyclone Wind Speed Retrieval from Dual-Polarization Sentinel-1 EW Mode Products

YUAN GAO, CHANGLONG GUAN, AND JIAN SUN

Physical Oceanography Laboratory, Ocean University of China, Qingdao, China

LIAN XIE

Department of Marine, Earth and Atmospheric Sciences, North Carolina State University, Raleigh, North Carolina

ABSTRACT

Recent studies indicate that the cross-polarization synthetic aperture radar (SAR) images have the ability of retrieving high wind speed on ocean surface without wind direction input. This study presents a new approach for tropical cyclone (TC) wind speed retrieval utilizing thermal-noise-removed Sentinel-1 dual-polarization (VV + VH) Extra-Wide Swath (EW) Mode products. Based on 20 images of 9 TCs observed in the 2016 and 2018 and SAR-collocated European Centre for Medium-Range Weather Forecasts (ECMWF) fifth-generation reanalysis (ERA5) data and the National Oceanic and Atmospheric Administration (NOAA) Hurricane Research Division's (HRD) Real-time Hurricane Wind Analysis System (H*Wind) data, a subswath-based geophysical model function (GMF) Sentinel-1 EW Mode Wind Speed Retrieval Model after Noise Removal (S1EW.NR) is developed and validated statistically. TC wind speed is retrieved by using the proposed GMF and the C-band model 5.N (CMOD5.N). The results show that the wind speeds retrieved by the S1EW.NR model are in good agreement with wind references up to 31 m s^{-1}. The correlation coefficient, bias, and standard deviation between the retrieval results and reference wind speeds are 0.74, −0.11, and 3.54 m s^{-1}, respectively. Comparison of the wind speeds retrieved from both channels suggests that the cross-polarized signal is more suitable for high–wind speed retrieval, indicating the promising capability of cross-polarization SAR for TC monitoring.

1. Introduction

Ocean surface wind speeds under tropical cyclone (TC) conditions are relevant to several climate variables, such as moisture, heat, and momentum fluxes between the ocean and atmosphere. A TC over ocean is always accompanied by severe wind, high sea state, and heavy cloud coverage, which increase the difficulty of wind speed monitoring. Since 1978, synthetic aperture radar (SAR) images with advantages of high spatial resolution, large spatial coverage, and the capability of sensing through clouds at day and night have become available for studying, forecasting, and monitoring TCs (Li 2015; Yu et al. 2017). With development of SAR technology, the TC wind speed retrieval by C-band SAR is widely studied from copolarization signals to cross-polarization (CP) signals (Zhang and Perrie 2014; Hwang 2016; Shao et al. 2017).

Generally, TC sea surface wind speed can be retrieved either from normalized radar cross section (NRCS) directly (Zhang and Perrie 2014; Zhang et al. 2017) or from the SAR-derived wave information indirectly (Hwang 2016; Shao et al. 2017). For TC conditions, due to the saturation of the drag coefficient, aerodynamic roughness, and sea surface roughness (Donelan et al. 2004; Bye and Jenkins 2006; Fujimura et al. 2019), the copolarization NRCS starts to saturate and decreases as wind speed increases beyond marginal hurricane strength (Hwang et al. 2010; Hwang and Fois 2015). This leads to ambiguous wind speed retrievals (Shen et al. 2009, 2016). Although the wind speed ambiguity can be removed (Shen et al. 2009), the current geophysical model functions (GMF) for copolarization SAR images are not sufficiently accurate in hurricane-force winds and can be applied only for retrieving wind speeds less than 25 m s^{-1} (Horstmann et al. 2005; Zhang et al. 2014; Mouche et al. 2017). In addition, the copolarization

---

 Denotes content that is immediately available upon publication as open access.

Corresponding author: Jian Sun, sunjian77@ouc.edu.cn

signal is dependent on wind direction, which is generally a priori input for wind speed retrieval, affecting the retrieval accuracy (Hersbach et al. 2007; Hersbach 2010).

Recent research on CP SAR images has shown that the CP NRCS is barely dependent upon wind direction and radar incident angle (Zhang et al. 2014, 2017; Gao et al. 2019). In addition, due to the ability of tracing wave breaking at moderate to high wind conditions, the CP signal remains sensitive to sea surface wind speed with high signal-to-noise ratio under TC conditions (Hwang and Fois 2015; Hwang et al. 2015). This overcomes the retrieval limitations of copolarization SAR images. Recently, several CP GMFs with respect to TC wind speed retrieval have been developed statistically for *RadarSat-2* (Hwang et al. 2010; Zhang and Perrie 2012; Van Zadelhoff et al. 2013, 2014; Zhang et al. 2014; Horstmann et al. 2015; Zhang et al. 2017), Sentinel-1 (Mouche et al. 2017; Gao et al. 2019), and *Gaofen-3* (Shao et al. 2018). The wind speeds retrieved from CP SAR images have significantly better performance than copolarization at wind speeds above $20\,\mathrm{m\,s^{-1}}$ (Horstmann et al. 2013; Mouche et al. 2017).

In 2019, according to 19 TC *Sentinel-1A* (*S-1A*) Extra-Wide Swath (EW) Mode VH-polarized (VH) images observed in 2016 and their collocated Soil Moisture Active Passive (SMAP) radiometer wind observations, Gao et al. analyzed the relationships between VH NRCS, sea surface wind speed, wind direction, and radar incident angle (Gao et al. 2019). The results show that the VH NRCS is mainly dependent on wind speed, barely dependent on incident angle, and independent of wind direction. In their paper, a basic GMF model and a corrected GMF model were proposed for each subswath and can be used to retrieve wind speeds up to $35\,\mathrm{m\,s^{-1}}$ for subswaths 1 to 4 and $25\,\mathrm{m\,s^{-1}}$ for subswath 5.

In this study, 20 Sentinel-1 (*S-1A* and *S-1B*) TC SAR images with TC eyes are studied for wind speed retrieval. The SAR-collocated wind speed data are collected from the European Centre for Medium-Range Weather Forecasts (ECMWF) fifth-generation reanalysis (ERA5) dataset, the National Oceanic and Atmospheric Administration (NOAA) Hurricane Research Division's (HRD) Real-time Hurricane Wind Analysis System (H*Wind), and SMAP observations. The research samples cover low-to-severe wind regimes ($2–31\,\mathrm{m\,s^{-1}}$). In the data preprocessing step, the thermal noise of SAR images is removed to correct the NRCS value, especially for subswaths 2 to 5. Based on the samples in training dataset and curve fitting, a new GMF Sentinel-1 EW Mode Wind Speed Retrieval Model after Noise Removal (S1EW.NR) is developed to provide an empirical relation between VH NRCS and wind speed. In addition, a new incident-angle-based correction methodology is utilized to eliminate the effect of incident angle on wind speed retrieval for subswath 1. Compared with the Sentinel-1 EW Mode Wind Speed Retrieval Model (S1EW) (Gao et al. 2019), the proposed GMF without wind direction parameter has much simpler form by summing subswaths 2 and 3 together and summing subswaths 4 and 5 together. For comparison between different channels, wind speeds are also retrieved from Sentinel-1 copolarization images, according to the well-validated GMF C-band model 5.N (CMOD5.N). Finally, the CP and copolarization retrieval results are validated with wind speeds from H*Wind, ERA5, and SMAP observations at different spatial resolutions.

This paper is organized as follows. Section 2 describes the Sentinel-1 imagery and reference wind data. In section 3, the relationships between VH NRCS, wind speed, and radar incident angle are analyzed. A new GMF is then proposed. In section 4, the proposed GMF is validated and compared with CMOD5.N and S1EW. Conclusions are summarized in section 5.

2. Dataset

In this study, 20 Sentinel-1 TC SAR images and their collocated wind references are divided into two datasets. Dataset 1 is a training dataset utilized for analyzing the relationships between VH NRCS, wind speed, and incident angle and proposing GMF. Dataset 2 is a testing dataset utilized for validation and comparison. Data information is shown in Table 1.

a. Sentinel-1 data

The SAR data studied in this paper are the Sentinel-1 EW Mode dual-polarization (VV + VH) Ground Range Detected (GRD) Medium-Resolution (MR) products, which are openly available from the European Space Agency (ESA). The Sentinel-1 is a C-band SAR mission designed by the ESA for ocean, land, and emergency services. It provides continuous all-weather, day-and-night imagery following a predefined mission planning. The Sentinel-1 has a constellation of two satellites: the *Sentinel-1A* launched in 2014 and the *Sentinel-1B* launched in 2016. In this study, seven TCs' SAR images are gathered by the Satellite Hurricane Observation Campaign (SHOC) during the 2016 hurricane season (Mouche et al. 2017).

The C-band SAR on board the Sentinel-1 satellites can be operated in four exclusive sensor modes with different resolution and coverage: the Stripmap Mode (SM), the Interferometric Wide Swath Mode (IW), the EW Mode, and the Wave Mode (WV) (Minchella 2016). For EW Mode images, the polarization scheme is single-polarization (HH or VV) or dual-polarization (VV + VH

TABLE 1. Data information.

Tropical cyclone name	Year	Instrument	No. of SAR images	Wind reference	Dataset
Gaston	2016	S-1A	6	ERA5 + SMAP	1 + 2
Hermine	2016	S-1A	2	ERA5 + SMAP	1 + 2
Lester	2016	S-1A	3	ERA5 + SMAP	1 + 2
Lionrock	2016	S-1A	2	ERA5 + SMAP	1 + 2
Megi	2016	S-1A	1	ERA5 + SMAP	1 + 2
Namtheun	2016	S-1A	1	ERA5	1
Karl	2016	S-1A	2	ERA5 + SMAP + H*Wind	2
Florence	2018	S-1A	2	ERA5	2
Helene	2018	S-1B	1	ERA5	2

or HH + HV). The Sentinel-1 level 1 products have two types: Single Look Complex (SLC) and Ground Range Detected. For GRD products, the focused SAR data have been detected, multilooked, and projected to ground range. The Level 1 GRD products are available in one of three spatial resolutions: full resolution (FR), high resolution (HR), and medium resolution. Each Sentinel-1 EW Mode GRD MR image has five subswaths (EW1, EW2, EW3, EW4, and EW5) covering incident angles from about 18.9° to 47.0° and is up to 410 km wide with a resolution of $93 \times 87\,\text{m}^2$ (range by azimuth) and a pixel spacing of $40 \times 40\,\text{m}^2$. The incident angles are about 19.75°–27.55°, 27.55°–32.55°, 32.55°–37.95°, 37.95°–42.85°, and 42.85°–46.95° for EW1 to EW5, respectively.

The operational observation mode of Sentinel-1 SAR is Terrain Observation with Progressive Scans SAR (TOPSAR). For CP channels of TOPSAR, the additive thermal noise power is further shaped by the application of postprocessing gains. The thermal noise is evident in CP images due to their lower NRCS. The thermal noise is hardly noticeable in copolarization channels, as the signal power is high enough to overwhelm the thermal noise (Gebert et al. 2010; Park et al. 2018). In this study, the Sentinel Application Platform 4.0 (SNAP 4.0) is applied for GRD border noise removal, thermal noise removal, and calibration. Figure 1 shows an example of an S-1A VH SAR image of Tropical Storm Karl between 2222
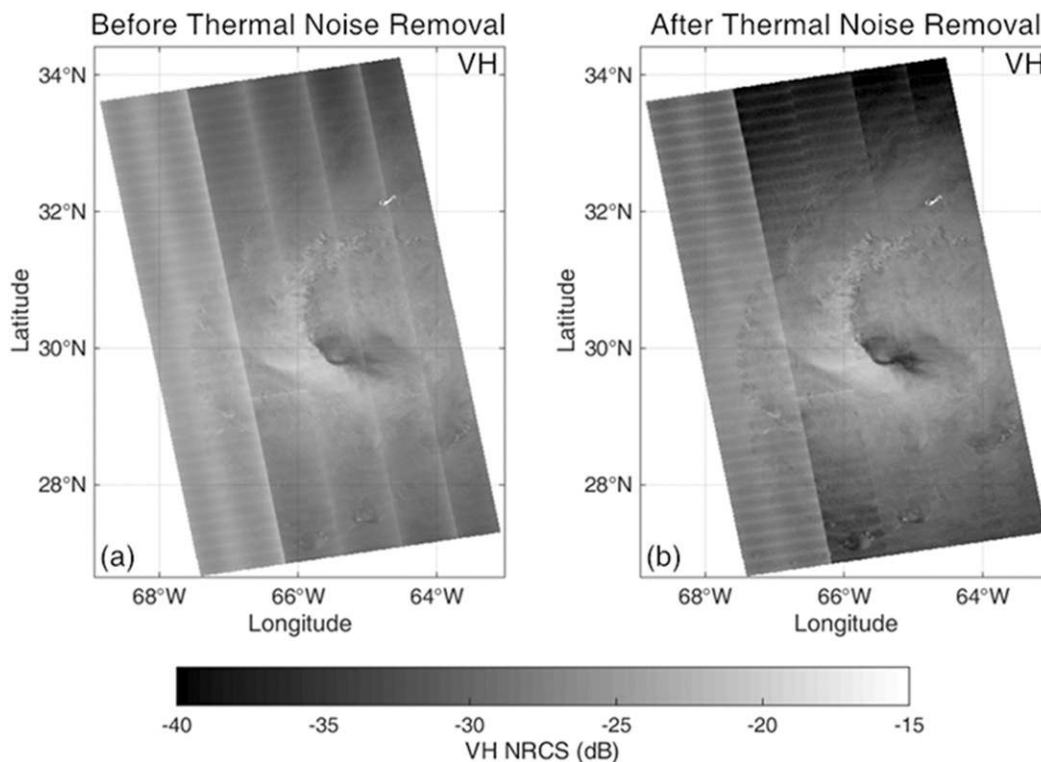

FIG. 1. Sentinel-1 VH NRCS maps of Tropical Storm Karl between 2222 and 2224 UTC 23 Sep 2016 (a) before and (b) after thermal noise removal.

and 2224 UTC 23 September 2016. After thermal noise removal (Fig. 1b), the high value of NRCS near interswath boundaries has been corrected. However, there are still some periodic streaks in range direction caused by scalloping burstwise variation (Park et al. 2018).

With respect to the SAR-collocated ERA5 wind speeds, Fig. 2 shows the distributions of VH NRCS in dataset 1 before thermal noise removal (Fig. 2a) and after thermal noise removal (Fig. 2b). The black curve stands for the noise equivalent sigma zero (NESZ) value, which is the smallest radar cross section that can be measured. After thermal noise removal, the minimum value of VH NRCS is lower than the NESZ. The maximum value of VH NRCS still remains high signal-to-noise ratio.

Due to the different spatial resolution between Sentinel-1 data and wind references, NRCS is averaged within each comparison cell for data matching. In this paper, a calculation resolution of 625×625 pixels is utilized for averaging, which is comparable to the spatial resolution of ERA5 data. The decrease in resolution (up to 25 km) does not dramatically change the homogeneity of NRCS and the sensitivity difference between VV and VH channels (Huang et al. 2017; Mouche et al. 2017; Gao et al. 2019).

b. Wind references

ERA5 is the fifth-generation ECMWF atmospheric reanalysis of the global climate, covering the period from 1950 to the present. Based on data assimilation, ERA5 combines model data with observations from across the world into a global dataset with an hourly temporal resolution and a horizontal resolution of $0.25° \times 0.25°$ (Hennermann and Berrisford 2017). ERA5 performs better than National Aeronautics and Space Administration (NASA) MERRA-2 in all analyzed aspects: correlations are higher, errors are in average around 20% lower, and distributions of both hourly data and changes in hourly data are more similar to those for measurements (Olauson 2018).

H*Wind is an integrated TC observing system providing the view of the extent and strength of hurricane wind field and used operationally to improve the damage assessment of hurricane intensity (Powell et al. 1998). An H*Wind analysis requires the input of all available surface weather observations with respect to the storm. In general, the total uncertainty of the H*Wind products in hurricanes is approximately 6% near the storm center, increasing to nearly 13% near the tropical storm force wind radius (DiNapoli et al. 2012). In this paper, the H*Wind data of Tropical Storm Karl are provided by Risk Management Solutions.
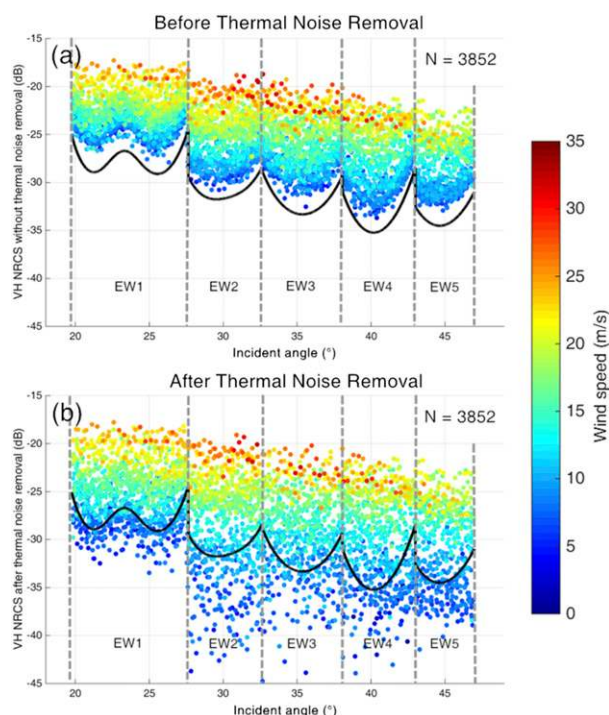

FIG. 2. The distributions between VH NRCS and incident angle under different wind speeds (a) before and (b) after thermal noise removal. The black curve is the NESZ value.

The spatial resolution of the H*Wind product used in this paper is $0.01° \times 0.01°$. The time step of the H*Wind product is 3 h.

The NASA SMAP level 2 wind speed is retrieved from brightness temperature measured by L-band passive radiometer. It has a spatial resolution of $0.25° \times 0.25°$ and a swath width of 1000 km. The revisit time of SMAP is 8 days. The root-mean-square difference (RMSD) with WindSat or Special Sensor Microwave Imager/Sounder is $1.7 \, \mathrm{m \, s^{-1}}$ for wind speeds lower than $20 \, \mathrm{m \, s^{-1}}$ (Yueh et al. 2016). The SMAP measurements also have a good agreement with the airborne Stepped Frequency Microwave Radiometer (SFMR) wind speeds with an RMSD of $4.6 \, \mathrm{m \, s^{-1}}$ for wind speeds between 20 and $40 \, \mathrm{m \, s^{-1}}$ (Yueh et al. 2016).

As is shown in Table 1, the SAR-collocated wind vectors at 10 m are collected from ERA5 dataset, H*Wind system, and SMAP observations. The time difference between SAR images and ERA5 data is controlled within half an hour. The time differences between SAR images of Tropical Storm Karl and H*Wind data are within 2 h. The sensing time difference between SAR images and SMAP data is within 1 h. Since there are few matching samples from the SFMR observations, experiments are only based on ERA5, H*Wind, and SMAP wind data.
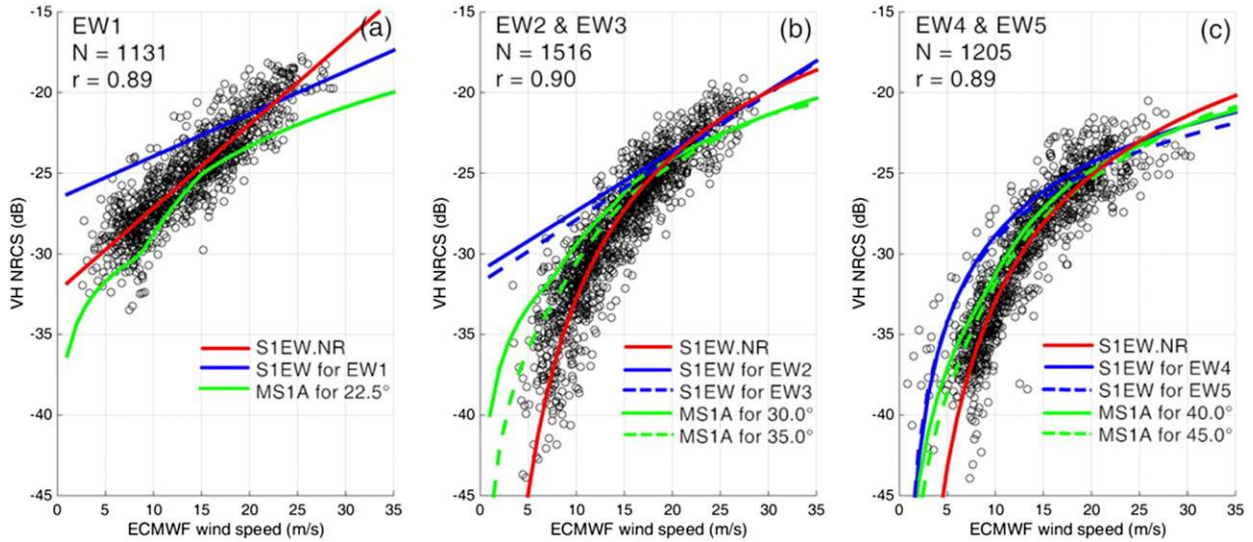
FIG. 3. Distributions of VH NRCS and wind speeds for (a) EW1, (b) EW2 and EW3, and (c) EW4 and EW5. The red, blue, and green curves represent the proposed S1EW.NR model, the S1EW model, and the MS1A model, respectively.

3. Methodology

To match up with the ERA5 data, the VH NRCS after thermal noise removal is averaged with a calculation resolution of $625 \times 16\,625$ pixels. For dataset 1, the latitude and longitude differences between SAR cells and ERA5 cells are controlled within $0.01°$ to establish the sample set. Then the VH NRCS, incident angle, and ERA5 wind vector of each sample are recorded and analyzed. Figure 3 shows the relationships between VH NRCS and wind speed in different subswaths. Due to the similar distributions of VH NCRS in EW2 and EW3 and in EW4 and EW5, the samples in two subswaths are gathered together for function fitting. The sample numbers are 1131, 1516, and 1205 for EW1, for EW2 and EW3, and for EW4 and EW5, respectively. The correlation coefficients r between VH NRCS and wind speed are 0.89, 0.90, and 0.89, indicating that appropriate fitting functions are able to simulate these distributions. In this study, the fitting functions are a linear function for EW1 and power-law functions for EW2 and EW3 and for EW4 and EW5. The fitting results are shown in Fig. 3 (red curves) and proposed as follows:

$$\sigma_0^W = \begin{cases} 0.52U_{10} - 32.34, & 19.75° \le \theta < 27.55° \\ -92.78U_{10}^{-0.45}, & 27.55° \le \theta < 37.95°, \\ -80.97U_{10}^{-0.39}, & 37.95° \le \theta < 46.95° \end{cases} \quad (1)$$

where σ_0^W stands for the VH NRCS (dB) after thermal noise removal, and U_{10} stands for the ocean surface wind speed (m s^{-1}) at 10-m height. The discontinuities of the proposed GMF can cause discontinuities in the wind

speed probability density functions (PDF). This will be discussed in section 4. Figure 3 shows a comparison of the proposed GMF S1EW.NR before incident angle correction with another two GMFs developed for Sentinel-1 EW Mode VH images, referred to as S1EW (blue curves) (Gao et al. 2019) and MS1A (green curves) (Mouche et al. 2017). Due to the different wind reference and preprocessing method of SAR data, three GMFs have large differences from each other, especially under low or high wind speeds.

After deriving these fitting functions, the simulated VH NRCS are calculated by the wind speeds of the training samples and then compared with the observed VH NRCS. The results are shown in Fig. 4. The
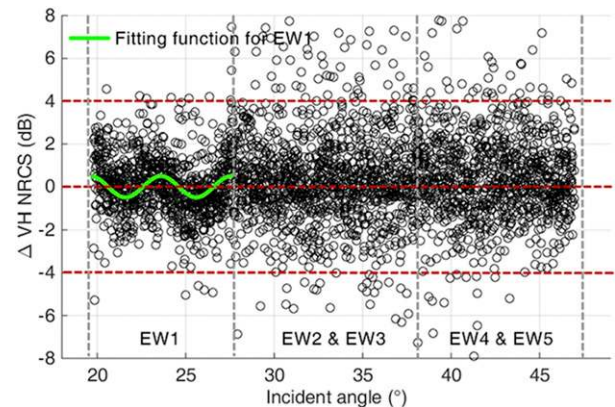

FIG. 4. The difference between simulated and observed VH NRCS before incident angle correction. The green curve is the fitting function for EW1.

difference between simulated VH NRCS and observed VH NRCS is calculated as

$$\Delta\sigma_0 = \sigma_0^{\text{Obs}} - \sigma_0^W, \tag{2}$$

where σ_0^{Obs} stands for the observed VH NRCS. There are 95% samples whose $\Delta\sigma_0$ are between -4 and $4\,\text{dB}$. For EW1, the fluctuation of $\Delta\sigma_0$ is similar to NESZ. As mentioned in section 2, it is mainly because the thermal noise is not eliminated thoroughly in EW1. However, for EW2–5, the mean $\Delta\sigma_0$ values are nearly 0, indicating that VH NRCS is independent of incident angle in these subswaths. In this study, trigonometric function is used to fit the relationship between mean $\Delta\sigma_0$ and incident angle for EW1. The fitting function is shown as green curve in Fig. 4.

Finally, the wind retrieval function for EW1 can be corrected with incident angle factor as follows:

$$\sigma_0^{\text{VH}} = \sigma_0^W + \Delta\sigma_0, \tag{3}$$

$$\Delta\sigma_0 = 0.50\sin(90.24\theta + 121.01), \quad 19.75° \le \theta < 27.55°, \tag{4}$$

where σ_0^{VH} is the VH NRCS in decibels after incident angle correction, and θ is the incident angle (°). For EW2–5, $\Delta\sigma_0$ is zero, and $\sigma_0^{\text{VH}} = \sigma_0^W$. Based on 3852 samples in dataset 1, experiment is made to compare the VH NRCS simulated by the S1EW.NR model [Eq. (3)] and the observed VH NRCS. The result is shown in Fig. 5. The correlation coefficient (r), bias, and standard deviation (Std) are 0.89, $-0.35\,\text{dB}$, and $2.40\,\text{dB}$, respectively. As thermal noise only affects the NRCS value at low-to-moderate wind regimes (0–$20\,\text{m\,s}^{-1}$), the incident angle correction function [Eq. (4)] can be only applied to low-to-moderate wind regimes. After thermal noise removal, due to the decrease of the VH NRCS near NESZ, the range of low wind speeds corresponds to a larger range of VH NRCS. As a result, the dispersity of these samples' simulations is big. However, it will not lead to a large error when the model is used for wind speed retrieval, because the slopes of the retrieval functions are big for low wind speeds.

4. Validation and comparison

As mentioned previously, the Sentinel-1 dual-polarization products provide both copolarization and CP SAR images. Based on dataset 2, the TC wind speeds are retrieved from both channels for comparison. In this paper, CMOD5.N is utilized to retrieve wind speeds from copolarization SAR images. CMOD5.N provides an empirical function between VV NRCS sensed by the *European Remote Sensing Satellite-2* (*ERS-2*) and
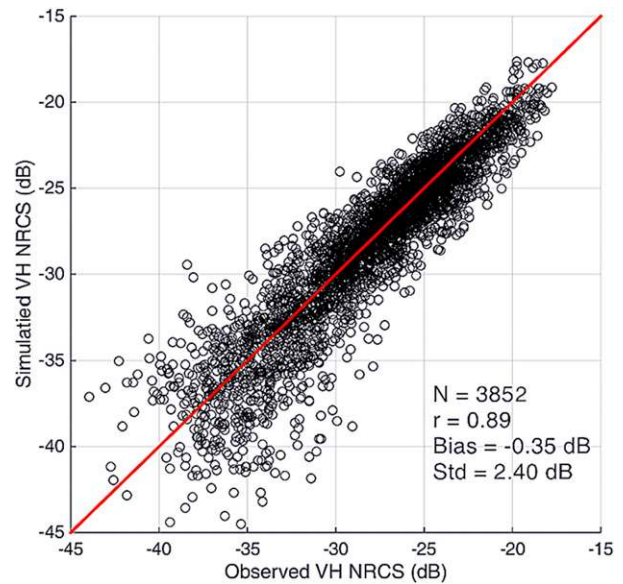

FIG. 5. Comparison between simulated and observed VH NRCS based on dataset 1.

Advanced Scatterometer (ASCAT) scatterometers and ocean surface vector wind at 10-m height. The wind speeds retrieved from ASCAT and *ERS-2* by CMOD5.N compare well on average with the operational neutral winds from ECMWF (Hersbach et al. 2007). CMOD5.N embodies a refit of CMOD5 and has a similar function to all the other CMOD models:

$$\sigma_0^{\text{VV}} = B_0(1 + B_1\cos\phi + B_2\cos2\phi)^{1.6}, \tag{5}$$

$$B_0 = 10^{a_0 + a_1 U_{10}} f(a_2 U_{10}, s_0)^\gamma, \tag{6}$$

$$B_1 = \frac{c_{14}(1+x) - c_{15}U_{10}\{0.5 + x - \tanh[4(x + c_{16} + c_{17}U_{10})]\}}{1 + \exp[0.34(U_{10} - c_{18})]}, \tag{7}$$

$$B_2 = (-d_1 + d_2v_2)\exp(-v_2), \tag{8}$$

$$x = \frac{\theta - 40}{25}, \tag{9}$$

where σ_0^{VV} is the VV NRCS (dB); B_i is the function of ocean surface wind speed and radar incident angle; ϕ is the angle between wind direction and SAR azimuth look angle in degrees; c_i is constant; and a_i, s_0, γ, d_i, and v_2 can be computed by c_i, x, and U_{10}. In this study, the wind direction information is acquired from H*Wind and ERA5 as external inputs.

A case study is made for Tropical Storm Karl (2016). The VV-polarized (VV) SAR image of Tropical Storm Karl is shown in Fig. 6. Figure 7 shows the SAR-retrieved wind speed maps between 2222 and 2224 UTC 23 September
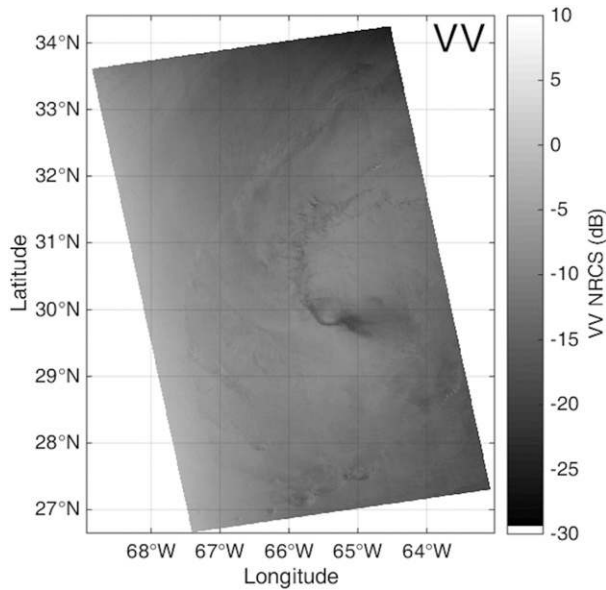
FIG. 6. Sentinel-1 VV NRCS map of Tropical Storm Karl between 2222 and 2224 UTC 23 Sep 2016.

With the benefit of high spatial resolution, Figs. 7a and 7b show the local information of Tropical Storm Karl's wind field structure. The differences between two SAR-retrieved wind maps are obvious for high wind speeds. As is shown in Fig. 6, the high VV signals are located below and above the storm eye. Therefore, for wind map retrieved from VV signals, the high–wind speed regions do not match up with the H*Wind map. In addition, its significant dispersity of high–wind speed regions is not realistic under TC conditions, according to the Holland model (Holland 1980; Xie et al. 2006). The outer wind speeds seem to be overestimated in Fig. 7a. These retrieval errors of CMOD5.N illustrate the influence of wind direction input on retrieval result. The wind map from VH signals is consistent very well with the H*Wind map, especially for the shape and location of high–wind speed regions near the storm eyewall. To note, the periodic streaks in Fig. 7b are caused by scalloping burstwise variation, which needs to be removed in further studies.

The scatterplots in Fig. 8 illustrate the comparison of SAR-retrieved wind speeds from both channels with H*Wind data and corresponding distributions of sample density. Due to the high spatial resolution of H*Wind data, there are 30 918 samples for comparison. The latitude and longitude differences between SAR cells and H*Wind cells are controlled within 0.001°. The samples cover wind speed range from 4 to 31 m s^{-1}.

2016 and corresponding H*Wind map of Tropical Storm Karl. Figure 7a is derived from VV signals by CMOD5.N. Figure 7b is derived from VH signals by the S1EW.NR model. According to NOAA HRD's track data, the location difference of Tropical Storm Karl's eye between SAR sensing time and H*Wind analysis time is 0.117° in latitude and 0.352° in longitude.
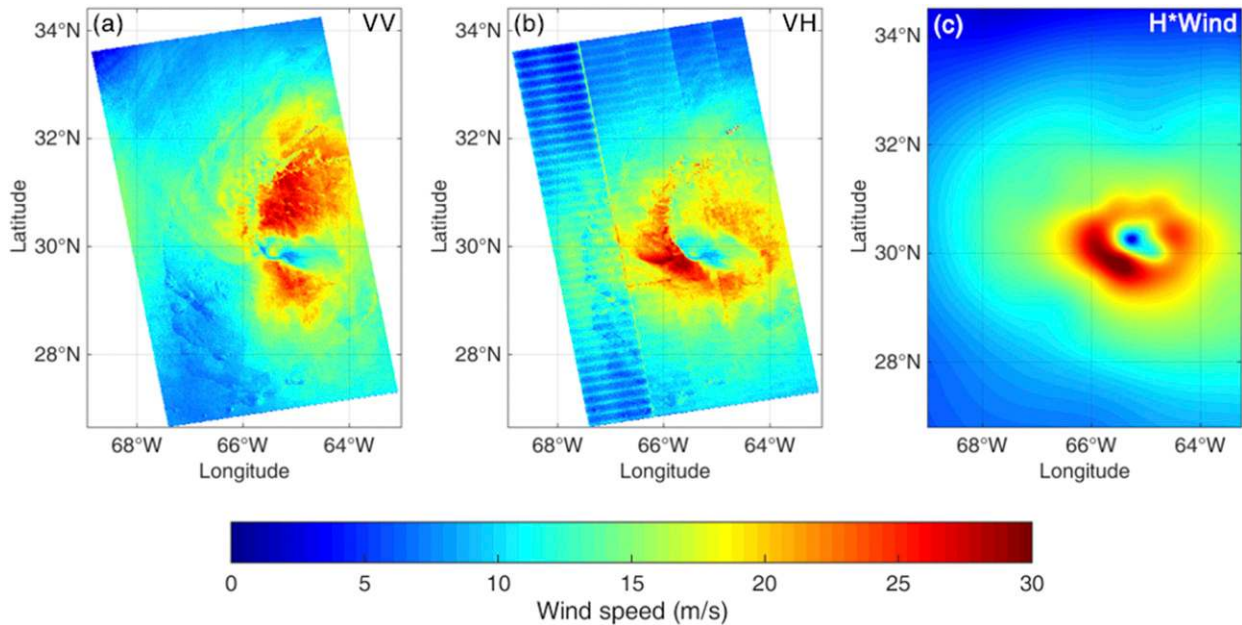

FIG. 7. Sentinel-1-retrieved ocean surface wind speed maps of Tropical Storm Karl between 2222 and 2224 UTC 23 Sep 2016 at 0.01° resolution using (a) VV signals and CMOD5.N and (b) VH signals and the S1EW.NR model. (c) SAR-collocated H*Wind ocean surface wind speed map at 2400 UTC 23 Sep 2016.
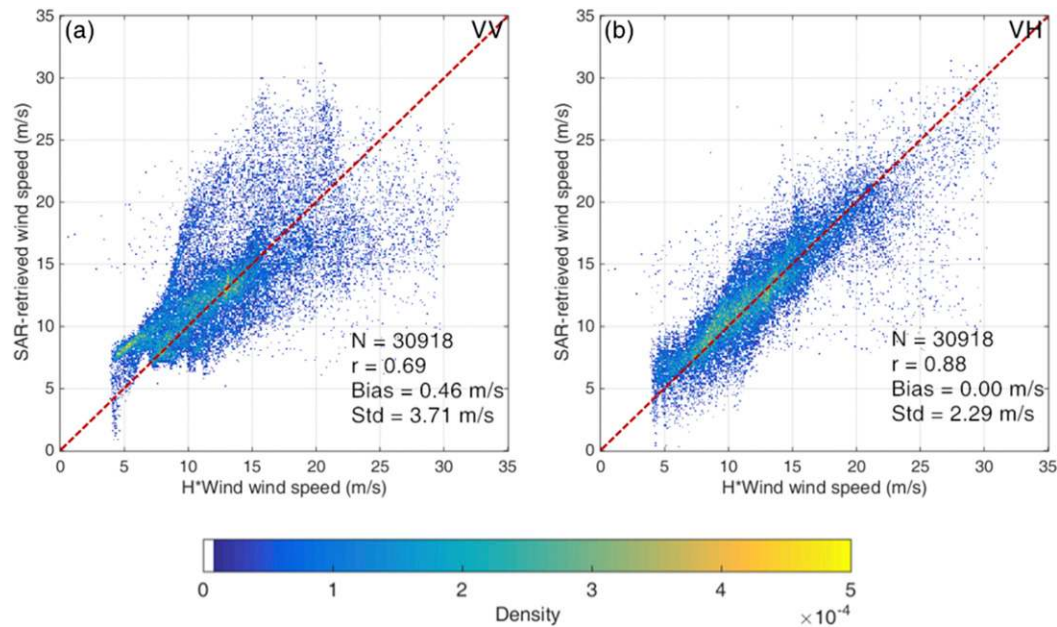
FIG. 8. Comparisons between H*Wind wind speeds and SAR-retrieved wind speeds of Tropical Storm Karl using (a) VV signals and CMOD5.N and (b) VH signals and the S1EW.NR model.

For VV results, the correlation coefficient, bias, and Std are 0.69, $0.46\,\mathrm{m\,s^{-1}}$, and $3.71\,\mathrm{m\,s^{-1}}$, respectively. On one hand, CMOD5.N underestimates the wind speeds higher than $20\,\mathrm{m\,s^{-1}}$, which is shown in Figs. 7a and 7c. This is because VV signals become saturated under high wind speeds. On the other hand, CMOD5.N overestimates low wind speeds ($<7\,\mathrm{m\,s^{-1}}$) by about $4\,\mathrm{m\,s^{-1}}$. For VH results, the correlation coefficient, bias, and Std are 0.88, $0.00\,\mathrm{m\,s^{-1}}$, and $2.29\,\mathrm{m\,s^{-1}}$. These results show that the TC wind speeds retrieved from VH signals have much higher accuracy than wind speeds retrieved from VV signals.

Since Sentinel-1 EW Mode imagery has five subswaths, discontinuities can be seen at interswath boundaries in VH images. The proposed S1EW.NR model is incident angle dependent and this leads to discontinuities in wind retrieval map. To evaluate this discontinuity, wind speed PDFs are calculated from the retrieval result and H*Wind data of Tropical Storm Karl. The PDFs on both sides of function boundaries are computed in a bin of 0.8°. In Fig. 9, it is clear that the PDFs of H*Wind wind speeds (red curves) are very similar in adjacent incident angle regions, while the PDFs of retrieval wind speeds are more different as expected, especially for interswath boundary of EW1 and EW2. Such discontinuity can also be seen in Fig. 7b. At interswath boundary of EW1 and EW2, the correlation coefficient of PDFs is 0.91 for retrieval result and 0.98 for H*Wind data. At interswath boundary of EW3 and EW4, the correlation coefficient of PDFs is 0.98 for retrieval result and 0.99 for H*Wind data. This means that discontinuity is greater at

interswath boundary of EW1 and EW2. These results show that discontinues GMF and swaths can cause discontinuities of wind speed PDF.

Under $0.25° \times 0.25°$ resolution, the same analysis has been performed to compare the S1EW.NR model and CMOD5.N. The wind directions used for CMOD5.N are acquired from ERA5. Retrieval maps and corresponding ERA5 wind map are shown in Fig. 10. In Figs. 10a and 10b, the locations of maximum wind speed are similar to Figs. 7a and 7b. However, the values of maximum wind speed retrieved from both signals are higher than the maximum wind speed from ERA5 by about $10\,\mathrm{m\,s^{-1}}$. According to the National Hurricane Center's (NHC) report, the maximum wind speed of Tropical Storm Karl was 55 kt ($28.29\,\mathrm{m\,s^{-1}}$) at the SAR sensing time. Obviously, the ERA5 underestimates the maximum wind speed for this case. Compared with H*Wind data, although the time of ERA5 data is closer to the SAR sensing time, the accuracy of ERA5 data is affected by smoothing of wind filed. For low–wind speed regions, the VV results are higher than VH results in the upper-left corner of the map and lower than VH results in the lower-left corner of the map. The different features of low–wind speed regions between this experiment and previous experiment illustrate the dependence of VV NRCS on wind direction.

In this study, experiment has also been made to retrieve wind speeds from the Sentinel-1 dual-polarization images of Hurricane Helene (2018) and Hurricane Florence (2019). The validation results are shown in Fig. 11. To note, in order to test the S1EW.NR model
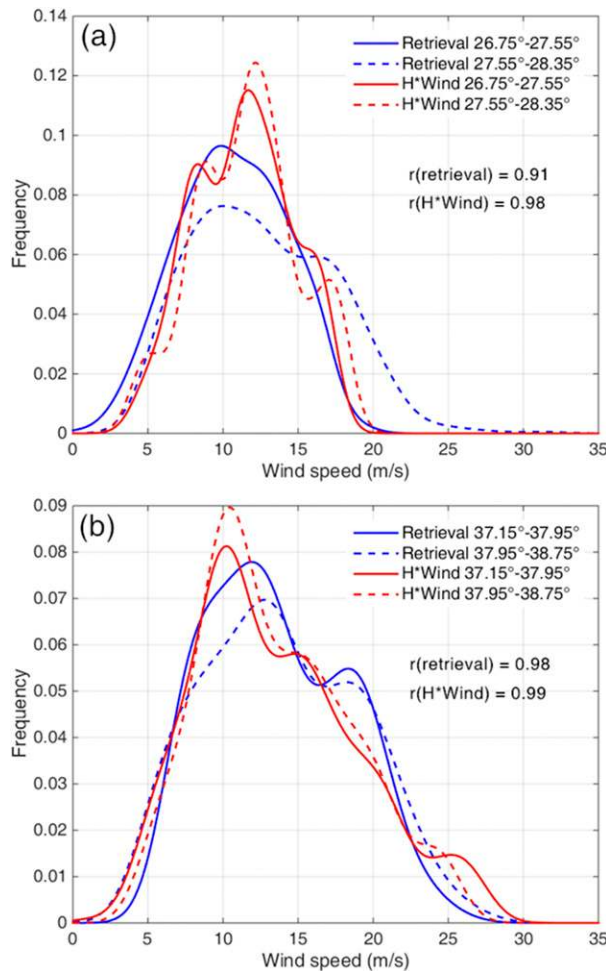
FIG. 9. Wind speed PDFs computed from retrieval result (blue) and H*Wind data (red) at interswath boundaries between (a) EW1 and EW2 and (b) EW3 and EW4.

and the S1EW.NR model perform well under moderate wind speeds. Compared with the previous experiment, low spatial resolution has negative influence on retrieval results.

As mentioned above, the proposed GMF is developed by ERA5 wind data and has been validated against model wind speeds from H*Wind and ERA5. To evaluate the correlation between retrieval results and observed wind speeds and compare the S1EW model and the S1EW.NR model, the SMAP measurements are collected in dataset 2 as wind speed references. The S1EW model is derived from SMAP wind speed observations and *S-1A* images and able to retrieve wind speeds from VH SAR images without thermal noise removal (Gao et al. 2019). Since the matching samples of the SMAP data are less than the ERA5 data, the SMAP data are only used for validation in this paper. As is shown in Fig. 12 and Table 1, there are 2664 matching samples for 14 SAR images in 5 TCs. The wind speeds range from 3 to $35\,\mathrm{m\,s^{-1}}$. The correlation coefficient, bias, and Std of VH results retrieved by the S1EW model are 0.86, $-0.17\,\mathrm{m\,s^{-1}}$, and $3.80\,\mathrm{m\,s^{-1}}$, respectively. The correlation coefficient, bias, and Std of VH results retrieved by the S1EW.NR model are 0.85, $0.20\,\mathrm{m\,s^{-1}}$, and $3.26\,\mathrm{m\,s^{-1}}$, respectively. The retrieval results of both models show good agreement with SMAP observations. For the wind speeds retrieved from the S1EW.NR model, its Std is 14% lower than the Std of S1EW-retrieved wind speeds. It indicates that the thermal noise removal could improve retrieval accuracy by reducing dispersity. However, the correlation coefficient and bias of the S1EW model are better than the S1EW.NR model because the S1EW model is fitted by these SMAP wind speeds (Gao et al. 2019).

5. Conclusions

This study illustrates that it is possible to retrieve TC ocean surface wind speed from both VV and VH SAR images of the Sentinel-1 satellites. The accuracy of wind speeds retrieved from VV SAR images is affected by prior input of wind direction and saturation of NRCS under high wind speed. However, VH NRCS is independent of wind direction and does not have saturation problem under high wind speed, indicating that it has great potential to retrieve wind speed with high accuracy under TC conditions. In addition, with the benefit of high spatial resolution, SAR images could be used to monitor local information of the TC structure.

In this paper, an empirical GMF has been presented for the thermal-noise-removed VH images of the Sentinel-1 dual-polarization EW Mode GRD products. Based on 20 SAR images and collocated ERA5 data

with the second instrument of Sentinel-1 mission, a SAR image of Hurricane Helene at 0818 UTC 12 September 2018 is collected from *Sentinel-1B* dataset. Two SAR images of Hurricane Florence are observed by *Sentinel-1A* at 2132 UTC 7 September 2018 and at 0939 UTC 8 September 2018. In 2018, Hurricane Florence caused major damage to the U.S. East Coast. Unfortunately, the Sentinel-1 images are only available for Florence at the tropical storm category. When considering 1226 samples, the correlation coefficient, bias, and Std of VV results are 0.63, $0.65\,\mathrm{m\,s^{-1}}$, and $4.28\,\mathrm{m\,s^{-1}}$, respectively. The correlation coefficient, bias, and Std of VH results are 0.74, $-0.11\,\mathrm{m\,s^{-1}}$, and $3.54\,\mathrm{m\,s^{-1}}$, respectively. The VH results are more consistent with ERA5 data. As expected, the low wind speeds retrieved by the S1EW.NR model have large Std due to the decrease of VH NRCS after thermal noise removal. According to the results of samples with high density (yellow dots in Fig. 11), both CMOD5.N
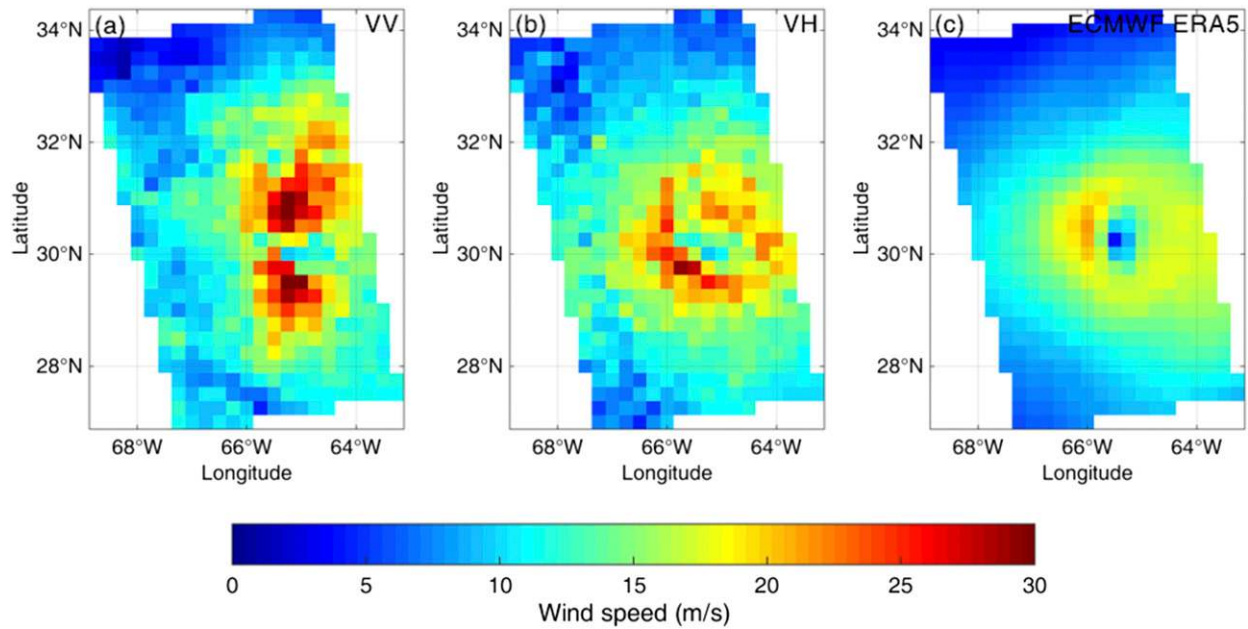
FIG. 10. Sentinel-1-retrieved ocean surface wind speed maps of Tropical Storm Karl between 2222 and 2224 UTC 23 Sep 2016 at 0.25° resolution using (a) VV signals and CMOD5.N, and (b) VH signals and the S1EW.NR model. (c) SAR-collocated ERA5 ocean surface wind speed map at 2200 UTC 23 Sep 2016.

under TC conditions, a subswath-based piecewise function is used to describe the relationship between VH NRCS and wind speed up to $35\,\mathrm{m\,s^{-1}}$. Compared with the S1EW model and MS1A model, the proposed S1EW.NR model has simpler structure and less

coefficients. In this new model, VH NRCS is dependent on wind speed and radar incident angle. For subswath 1, due to the effect of the remainder thermal noise, the S1EW.NR model has been corrected by a sine function of incident angle.
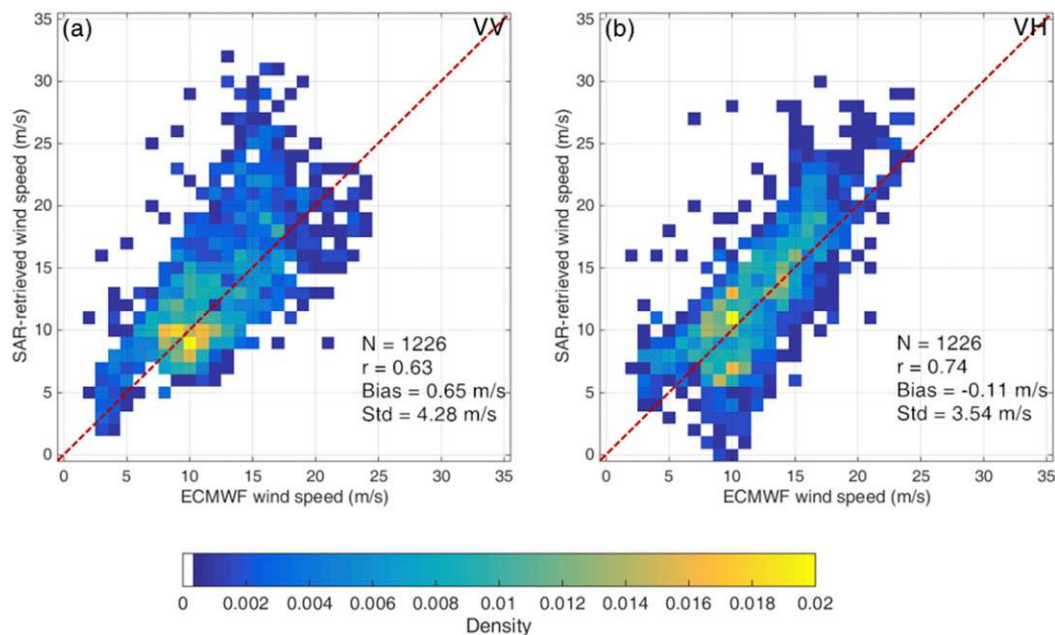

FIG. 11. Comparisons between ERA5 wind speeds and SAR-retrieved wind speeds of Tropical Storm Karl, Hurricane Helene, and Tropical Storm Florence using (a) VV signals and CMOD5.N and (b) VH signals and the S1EW.NR model.
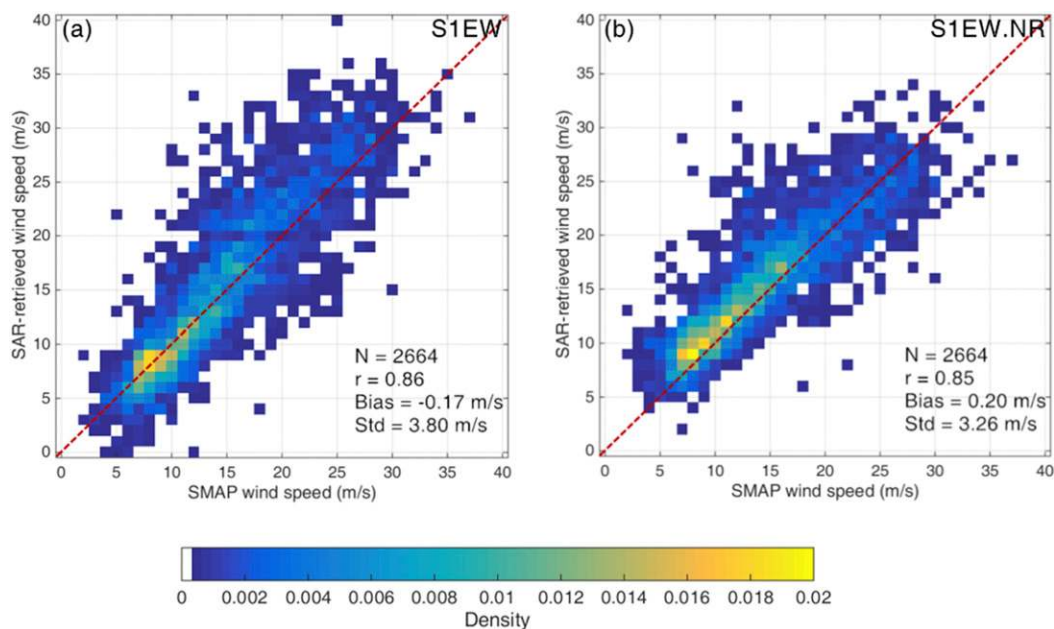
FIG. 12. Comparisons between SMAP wind speeds and SAR-retrieved wind speeds using (a) the S1EW model and (b) the S1EW.NR model.

In this paper, the S1EW.NR model is validated with both observed wind data and model wind data at two different spatial resolutions. The proposed model is also compared with the copolarization radar GMF CMOD5.N. According to the case study of Tropical Storm Karl, the wind speed map retrieved by the S1EW.NR model is more consistent with the SAR-collocated H*Wind map than the result retrieved by CMOD5.N. For VV retrieval results, the correlation coefficient, bias, and Std are 0.69, 0.46 m s^{-1}, and 3.71 m s^{-1}, respectively. For VH retrieval results, the correlation coefficient, bias, and Std are 0.88, 0.00 m s^{-1}, and 2.29 m s^{-1}, respectively. Validation and comparison are made to test the S1EW.NR model by the Sentinel-1 images of Hurricane Helene and Tropical Storm Florence and the corresponding ERA5 data. For VV retrieval results, the correlation coefficient, bias, and Std are 0.63, 0.65 m s^{-1}, and 4.28 m s^{-1}, respectively. For VH retrieval results, the correlation coefficient, bias, and Std are 0.74, -0.11 m s^{-1}, and 3.54 m s^{-1}, respectively. In this paper, the S1EW.NR model is tested by the SMAP wind observations, the correlation coefficient, bias, and Std are 0.85, 0.20 m s^{-1}, and 3.26 m s^{-1}, respectively. Results show that the S1EW.NR model is more accurate and reliable than CMOD5.N and has smaller Std than the S1EW model for TC wind speed retrieval. In addition, the retrieval results at two different spatial resolutions indicate that both the S1EW.NR model and CMOD5.N perform better at higher spatial resolution.

REFERENCES

Bye, J. A., and A. D. Jenkins, 2006: Drag coefficient reduction at very high wind speeds. *J. Geophys. Res.*, **111**, C03024, https://doi.org/10.1029/2005JC003114.

DiNapoli, S. M., M. A. Bourassa, and M. D. Powell, 2012: Uncertainty and intercalibration analysis of H*Wind. *J. Atmos. Oceanic Technol.*, **29**, 822–833, https://doi.org/10.1175/JTECH-D-11-00165.1.

Donelan, M. A., B. K. Haus, N. Reul, W. J. Plant, M. Stiassnie, H. C. Graber, O. B. Brown, and E. S. Saltzman, 2004: On the limiting aerodynamic roughness of the ocean in very strong winds. *Geophys. Res. Lett.*, **31**, L18306, https://doi.org/10.1029/2004GL019460.

Fujimura, A., S. Lehner, A. Soloviev, and X. Li, 2019: Sea surface roughness observed by high resolution radar. *Remote Sens.*, **11**, 2026, https://doi.org/10.3390/rs11172026.

Gao, Y., C. Guan, J. Sun, and L. Xie, 2019: A wind speed retrieval model for Sentinel-1A EW mode cross-polarization images. *Remote Sens.*, **11**, 153, https://doi.org/10.3390/rs11020153.

Gebert, N., G. Krieger, and A. Moreira, 2010: Multichannel azimuth processing in ScanSAR and TOPS mode operation. *IEEE Trans. Geosci. Remote Sens.*, **48**, 2994–3008, https://doi.org/10.1109/TGRS.2010.2041356.

Hennermann, K., and P. Berrisford, 2017: ERA5 data documentation. Copernicus Knowledge Base, https://confluence.ecmwf.int/display/CKB/ERA5%3A+data+documentation.

Hersbach, H., 2010: Comparison of C-band scatterometer CMOD5.N equivalent neutral winds with ECMWF. *J. Atmos. Oceanic Technol.*, **27**, 721–736, https://doi.org/10.1175/2009JTECHO698.1.

——, A. Stoffelen, and S. de Haan, 2007: An improved C-band scatterometer ocean geophysical model function: CMOD5. *J. Geophys. Res.*, **112**, C03006, https://doi.org/10.1029/2006JC003743.

Holland, G. J., 1980: An analytic model of the wind and pressure profiles in hurricanes. *Mon. Wea. Rev.*, **108**, 1212–1218, https://doi.org/10.1175/1520-0493(1980)108<1212:AAMOTW>2.0.CO;2.

Horstmann, J., D. R. Thompson, F. Monaldo, S. Iris, and H. C. Graber, 2005: Can synthetic aperture radars be used to estimate hurricane force winds? *Geophys. Res. Lett.*, **32**, L22801, https://doi.org/10.1029/2005GL023992.

——, C. Wackerman, R. Foster, M. Caruso, and H. Graber, 2013: Tropical cyclone winds retrieved from synthetic aperture radar. *Oceanography*, **26**, 46–57, https://doi.org/10.5670/oceanog.2013.30.

——, S. Falchetti, C. Wackerman, S. Maresca, M. J. Caruso, and H. C. Graber, 2015: Tropical cyclone winds retrieved from C-band cross-polarized synthetic aperture radar. *IEEE Trans. Geosci. Remote Sens.*, **53**, 2887–2898, https://doi.org/10.1109/TGRS.2014.2366433.

Huang, L., B. Liu, X. Li, Z. Zhang, and W. Yu, 2017: Technical evaluation of Sentinel-1 IW mode cross-pol radar backscattering from the ocean surface in moderate wind condition. *Remote Sens.*, **9**, 854, https://doi.org/10.3390/rs9080854.

Hwang, P. A., 2016: Fetch- and duration-limited nature of surface wave growth inside tropical cyclones: With applications to air–sea exchange and remote sensing. *J. Phys. Oceanogr.*, **46**, 41–56, https://doi.org/10.1175/JPO-D-15-0173.1.

——, and F. Fois, 2015: Surface roughness and breaking wave properties retrieved from polarimetric microwave radar backscattering. *J. Geophys. Res. Oceans*, **120**, 3640–3657, https://doi.org/10.1002/2015JC010782.

——, B. Zhang, and W. Perrie, 2010: Depolarized radar return for breaking wave measurement and hurricane wind retrieval. *Geophys. Res. Lett.*, **37**, L01604, https://doi.org/10.1029/2009GL041780.

——, A. Stoffelen, G. J. Zadelhoff, W. Perrie, B. Zhang, H. Li, and H. Shen, 2015: Cross-polarization geophysical model function for C-band radar backscattering from the ocean surface and wind speed retrieval. *J. Geophys. Res. Oceans*, **120**, 893–909, https://doi.org/10.1002/2014JC010439.

Li, X., 2015: The first Sentinel-1 SAR image of a typhoon. *Acta Oceanol. Sin.*, **34** (1), 1–2, https://doi.org/10.1007/s13131-015-0589-8.

Minchella, A., 2016: Sentinel-1 overview. *Proc. ESA SNAP-Sentinel-1 Training Course*, Hartwell, United Kingdom, Satellite Applications Catapult, http://s3-eu-west-1.amazonaws.com/media.newsa.catapult/wp-content/uploads/2019/01/15094323/SNAP-Sentinel-1_TrainingCourse_OverviewSentinel-1.pdf.

Mouche, A. A., B. Chapron, B. Zhang, and R. Husson, 2017: Combined co- and cross-polarized SAR measurements under extreme wind conditions. *IEEE Trans. Geosci. Remote Sens.*, **55**, 6746–6755, https://doi.org/10.1109/TGRS.2017.2732508.

Olauson, J., 2018: ERA5: The new champion of wind power modelling? *Renewable Energy*, **126**, 322–331, https://doi.org/10.1016/j.renene.2018.03.056.

Park, J. W., A. A. Korosov, M. Babiker, S. Sandven, and J. S. Won, 2018: Efficient thermal noise removal for Sentinel-1 TOPSAR cross-polarization channel. *IEEE Trans. Geosci. Remote Sens.*, **56**, 1555–1565, https://doi.org/10.1109/TGRS.2017.2765248.

Powell, M. D., S. H. Houston, L. R. Amat, and N. Morisseau-Leroy, 1998: The HRD real-time hurricane wind analysis system. *J. Wind Eng. Ind. Aerodyn.*, **77–78**, 53–64, https://doi.org/10.1016/S0167-6105(98)00131-7.

Shao, W., X. Li, P. Hwang, B. Zhang, and X. Yang, 2017: Bridging the gap between cyclone wind and wave by C-band SAR measurements. *J. Geophys. Res. Oceans*, **122**, 6714–6724, https://doi.org/10.1002/2017JC012908.

——, X. Yuan, Y. Sheng, J. Sun, W. Zhou, and Q. Zhang, 2018: Development of wind speed retrieval from cross-polarization Chinese Gaofen-3 synthetic aperture radar in typhoons. *Sensors*, **18**, 412, https://doi.org/10.3390/s18020412.

Shen, H., Y. He, and W. Perrie, 2009: Speed ambiguity in hurricane wind retrieval from SAR imagery. *Int. J. Remote Sens.*, **30**, 2827–2836, https://doi.org/10.1080/01431160802555879.

——, W. Perrie, and Y. He, 2016: Evaluation of hurricane wind speed retrieval from cross-dual-pol SAR. *Int. J. Remote Sens.*, **37**, 599–614, https://doi.org/10.1080/01431161.2015.1134845.

Van Zadelhoff, G. J., A. Stoffelen, P. W. Vachon, J. Wolfe, J. Horstmann, and M. Belmonte Rivas, 2013: Scatterometer hurricane wind speed retrievals using cross polarization. *Atmos. Meas. Tech. Discuss.*, **6**, 7945–7984, https://doi.org/10.5194/amtd-6-7945-2013.

——, ——, ——, ——, ——, and ——, 2014: Retrieving hurricane wind speeds using cross-polarization C-band measurements. *Atmos. Meas. Tech.*, **7**, 437–449, https://doi.org/10.5194/amt-7-437-2014.

Xie, L., S. Bao, L. J. Pietrafesa, K. Foley, and M. Fuentes, 2006: A real-time hurricane surface wind forecasting model: Formulation and verification. *Mon. Wea. Rev.*, **134**, 1355–1370, https://doi.org/10.1175/MWR3126.1.

Yu, Y., X. Yang, W. Zhang, B. Duan, X. Cao, and H. Leng, 2017: Assimilation of Sentinel-1 derived sea surface winds for typhoon forecasting. *Remote Sens.*, **9**, 845, https://doi.org/10.3390/rs9080845.

Yueh, S. H., A. G. Fore, W. Tang, A. Hayashi, B. Stiles, N. Reul, Y. Weng, and F. Zhang, 2016: SMAP L-band passive microwave observations of ocean surface wind during severe storms. *IEEE Trans. Geosci. Remote Sens.*, **54**, 7339–7350, https://doi.org/10.1109/TGRS.2016.2600239.

Zhang, B., and W. Perrie, 2012: Cross-polarized synthetic aperture radar: A new potential measurement technique for hurricanes. *Bull. Amer. Meteor. Soc.*, **93**, 531–541, https://doi.org/10.1175/BAMS-D-11-00001.1.

——, and ——, 2014: Recent progress on high wind-speed retrieval from multi-polarization SAR imagery: A review. *Int. J. Remote Sens.*, **35**, 4031–4045, https://doi.org/10.1080/01431161.2014.916451.

——, ——, J. A. Zhang, E. W. Uhlhorn, and Y. He, 2014: High-resolution hurricane vector winds from C-band dual-polarization SAR observations. *J. Atmos. Oceanic Technol.*, **31**, 272–286, https://doi.org/10.1175/JTECH-D-13-00006.1.

Zhang, G., X. Li, W. Perrie, P. A. Hwang, B. Zhang, and X. Yang, 2017: A hurricane wind speed retrieval model for C-band RADARSAT-2 cross-polarization ScanSAR images. *IEEE Trans. Geosci.*, **55**, 4766–4774, https://doi.org/10.1109/TGRS.2017.2699622.